Optics & Laser Technology 156 (2022) 108596

Contents lists available at ScienceDirect

Optics and Laser Technology

journal homepage: www.elsevier.com/locate/optlastec

Full length article

Backflow-assisted time-resolved phase modulation in nematic liquid crystal Pi-Cells

Yihan Jin, Steve J. Elston, Julian A.J. Fells, Bohan Chen, Mengmeng Li, Waqas Kamal, Zimo Zhao, Stephen M. Morris *

Department of Engineering Science, University of Oxford, Parks Road, Oxford OX1 3PJ, United Kingdom

ARTICLE INFO

Keywords:
Optical phase measurement
Liquid crystal
Analogue phase modulation
Submillisecond

ABSTRACT

By monitoring the time-dependent phase modulation behavior, we demonstrate the benefits of backflow on the phase modulation depth of nematic liquid crystal (LC) pi-cells in comparison to the phase modulation observed for other nematic LC device configurations. Specifically, results are presented for the time-resolved phase modulation of three different nematic LC device configurations under a range of electric field conditions: pi-cell (parallel-rubbed alignment layers), Fréedericksz cell (anti-parallel rubbed alignment layers), and a hybrid aligned nematic (HAN) device. The time-dependent behavior is obtained experimentally with a Michelson interferometer with a piezoelectric scanning mirror in the reference arm, which provides a continuous phase ramp in the reference signal. By recording the interference signal intensity, it is then possible to extract the change in optical phase as a function of time. It is shown that both the pi-cell and Fréedericksz cell exhibit a modulation that is greater than π radians for a double-pass configuration (2π radians for a four-pass configuration), with the lowest voltage amplitude corresponding to π phase modulation being observed for the pi-cell. Through the time-resolved response, it is shown that the presence of backflow hinders the dynamic phase response of the Fréedericksz device but does not negatively impact the behavior of the pi-cell. These results are found to be in good agreement with simulations of the phase modulation for the three nematic devices when backflow is taken into consideration.

1. Introduction

Liquid crystal (LC) spatial light modulators (SLMs) have become an enabling technology for shaping the wavefront of light in a range of different applications including laser micromachining [1], optical communications [2], and biomedical imaging [3]. Phase-only optical modulation, in particular, is found to be important for augmented reality (AR) near-eye displays [4–7] and free-space optical beam steering [8–10]. A key reason why LC-SLM technology is of significant value is that it enables direct control over the structure of the optical illumination through the application of a voltage to a thin pixelated LC layer. When considering which LC phase to use in SLMs, the choice has historically been between nematic [11] and ferroelectric [12] materials, although other LC phases have been considered in recent years [13].

In terms of the technology requirements for current commercial applications, both the nematic and ferroelectric phases have their advantages and disadvantages, such as depth of modulation versus speed, and the trade-off between these properties depends upon the nature of the application. Ferroelectric LC (FLC) devices can be operated in a number of different modes, but it is common in SLM applications to use them in a bistable configuration. Depending on the choice of input and output optical polarisation states this then allows either amplitude modulation or phase modulation or a combination of the two to be realised. For example, early work on the development of FLC devices for optical modulation demonstrated that they can switch between two states using a surface stabilised FLC arrangement [14]. Alternatively, a more recent report has demonstrated free space adaptive optical interconnects operating at 1.25 Gb/s using a bistable FLC-SLM that can provide a retardation of approximately 0.8π at 850 nm [15]. A critical feature that is essential for AR display applications as well as for optical communications is the switching speed, which is determined by both the LC phase that is used and the fundamental configuration of the LC layer (e.g., the alignment of the director in the case of a nematic LC). In the case of nematic LC devices that consist of anti-parallel rubbed planar

* Corresponding author.
E-mail addresses: steve.elston@eng.ox.ac.uk (S.J. Elston), stephen.morris@eng.ox.ac.uk (S.M. Morris).

https://doi.org/10.1016/j.optlastec.2022.108596
Received 22 April 2022; Received in revised form 2 August 2022; Accepted 14 August 2022
Available online 26 August 2022

alignment layers (e.g., rubbed polyimide), the result is a uniformly-aligned nematic LC layer with the director aligned approximately parallel to the device substrates. When an electric field is applied, and for a positive dielectric anisotropy nematic LC, the director rotates to align with the electric field. The threshold voltage above which the LC director reorients is known as the Fréedericksz transition. Due to the two different principal refractive indices along and perpendicular to the director, the result is a modification in the effective birefringence, which in turn alters the difference in the optical path length and consequently the phase difference, thus making optical phase modulation possible.

In a practical device application, analogue phase modulation is generally much more useful than bi-state modulation, which in turn requires a continuous rotation of the LC director under an applied electric field. The detailed device behavior is complicated by the various physical processes that take place during switching, which are influenced by both the material and device behavioral properties such as the elasticity, viscosity, and backflow. Combined with the initial device configuration, these properties determine the speed of the phase modulation and thus have significant impact on the switching speed of the LC-SLMs [16]. For example, flow-reorientation coupling in nematic director switching (commonly referred to as backflow) tends to slow down the switch-off process in nematic LC based device technology. This is because during switch-off the director reorientation-induced flow of the LC tends to work against the required reorientation process, slowing down the behavior. This is unfortunate because slow modulation impedes access to higher information bandwidths and limits high-speed applications – for example, this can result in breakup in field sequential color operation [17]. Understanding the time-resolved response of the phase modulation is therefore of crucial importance in terms of improving the response time and selecting the best-performing configurations. This, in turn, requires a direct measurement of the time-resolved response of the optical phase modulation of these LC phase modulators.

Whilst in many of the practical applications involving LC phase modulation, such as in SLMs, it is the relative phase of the propagating wavefront between different pixels which is important, in order to study phase modulation behavior directly it is beneficial to measure the induced phase change relative to a reference wave. A convenient way to do this is, for example, to use a Michelson interferometer whereby the LC device to be investigated is placed in one "arm" of the interferometer. Other methods that have been explored include Young's double slit configuration [18] or by introducing a Ronchi grating in the object plane and observing the variation in the diffraction pattern in the imaging plane so as to infer the phase modulation depth [19]. Another approach is to use a Twyman-Green interferometer, which can provide quantitative information about the phase shift [20,21]. In our previous work, we have tracked the changes in the phase by imaging the interference fringes [22]. However, this method is not ideal because for LC devices that reorient at millisecond timescales it is necessary to use either high speed imaging of the fringes or else to use a stroboscopic imaging approach. Additionally, the process of phase modulation extraction from the data, through image processing and fitting of line samples from images, adds additional complexity and potential sources of error, particularly as highly uniform images of the fringes are required.

To address these issues a measurement of the phase as a function of time is needed. We recently developed a heterodyne interferometer to measure optical phase over time [23]. In this paper we use a variation on this approach, such that a piezoelectric scanning mirror is placed in the reference arm of a Michelson interferometer to provide a continuous phase ramp in the reference signal. The interference signal intensity is then recorded and the phase modulation can be extracted directly. We then use this technique to investigate the time-dependent phase modulation behavior for three technologically-important nematic LC alignments which are shown in Fig. 1. In Fig. 1 (a) we illustrate anti-parallel rubbed planar aligned nematic LC (we refer to this as the Fréedericksz cell) [24] - this is actually the most commonly used nematic alignment in phase modulation nematic SLMs. In Fig. 1 (b) we illustrate parallel-rubbed planar alignment (the pi-cell configuration) [24] – this has been shown to exhibit fast switching. Early work on this operating mode showed that the relaxation time from the switched state to the bend state (shown as the $\vec{E}$ on and $\vec{E}$ off states in Fig. 1 (b)) could take place on millisecond time scales [25]. Further investigations showed that the unique geometry of the pi-cell configuration allows more favourable nematic director switching dynamics (flow-reorientation coupling) than other switching modes, enhancing the switching speed and making the mode potentially useful for high-speed applications such as field-sequential color displays [26,27]. This mode is therefore also interesting for current and future optical phase modulation technologies. In Fig. 1 (c) a hybrid aligned nematic (HAN) [28] cell arrangement is shown.

In this work, we compare our experimental findings with simulations of the phase modulation behavior when backflow is considered and combine the effect of backflow with the elasticity and viscosity properties that are typically discussed in the context of response time studies. By modelling the influence of backflow for these three different nematic LC device configurations, and making comparisons with experiments, it is possible to identify the optimum configurations and understand their resultant behavior. These dynamic phase response measurements demonstrate that backflow hinders the response of the Fréedericksz cell but not the response for the pi-cell. The findings and experimental technique presented would be of importance for commercial LC devices and could, in the future, lead to the development of faster, analogue phase-only modulation.

2. Experiment and simulation

2.1. Experiment configuration

A schematic of the Michelson interferometer that is equipped with the piezoelectric scan mirror arrangement used in this study is shown in Fig. 2. A continuous wave He-Ne laser (Thorlabs, HNL505L) operating at 632.8 nm is passed through a 50:50 beam splitter (Thorlabs, BS016-50:50 Non-Polarizing Beamsplitter Cube, 400–700 nm, 20 nm) where the beam is split into two: one beam passes through a linear polarizer and then the LC device under test before being reflected back by a mirror. The orientation of the LC device is with the surface alignment direction parallel to the incident polarizer in order to lead to optimum

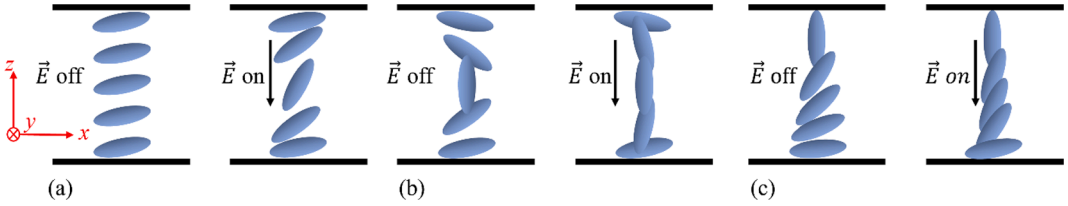

Fig. 1. Illustration of the three different configurations of the LC director for the nematic LC devices considered in this work: (a) Fréedericksz device (anti-parallel rubbed alignment layers); (b) pi-cell (parallel-rubbed alignment layers); (c) HAN device. All configurations are shown with and without an applied electric field. It is considered that the director only rotates within the x-z plane.

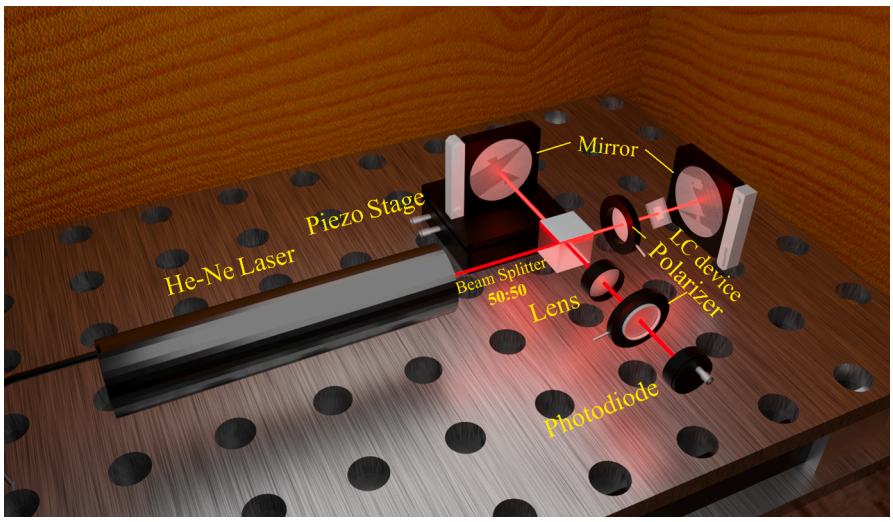

Fig. 2. A schematic illustration of the Michelson interferometer with a piezoelectric scan mirror placed in one arm of the interferometer.

phase modulation. The other beam, on the other hand, propagates towards a second mirror that is mounted on a piezoelectric stage (Melles Griot, 17 TFJ001/D) that is controlled by a waveform generator (Multicomp PRO, MP750510) via a Melles Griot Piezoelectric Controller (17 PCW002). By carefully adjusting the frequency, shape and amplitude of the control waveform, the piezoelectric stage that is fitted with the mirror can move along the optical axis back and forth smoothly. The piezoelectric stage is controlled by a triangular waveform with a 10 % symmetry, 30 mHz frequency so that the mirror travels from 30 μm to 35 μm (the total travel distance of the piezo stage is 50 μm and has a good linearity between 8 μm and 45 μm) over a period of 30 s.

The principle of this method is generally referred to as phase shifting interferometry. This approach can be used in a range of applications, such as in axial surface and position measurements and in high resolution interference microscopy [29–31]. The method is generally based on changing the optical path length smoothly and continuously in the reference arm, resulting in intensity in the interference pattern which will continuously change. The resulting signal (or series of images in an imaging system) can then be analysed to extract the required phase information. For example, in our system this approach leads to a sine wave profile being captured for a fixed signal beam phase. The frequency of this sine wave depends on the characteristics of the movement of the scanning stage. The LC phase modulator under investigation is then controlled by an external waveform signal. The phase shift waveform from the signal arm will then effectively be overlaid on top of the sine wave to form a new waveform with a different shape. By selecting, extracting, and analysing the new waveform at some key feature points, we can then extract the value of the phase shift, as explained in the analysis in the next section. The material chosen for this investigation is the widely studied LC nematic mixture E7 (Synthon Chemicals ltd.). The clearing temperature of this mixture is 58 °C [32] and the ordinary and extraordinary refractive indices are $n_o = 1.52$ and $n_e = 1.74$ [33], respectively, at a wavelength of 632.8 nm and room temperature. The dielectric anisotropy of E7 at room temperature is reported to be $\Delta\varepsilon \approx 14$.

2.2. Theoretical considerations

2.2.1. Extraction of the optical phase

In general, the single point intensity observed on an imaging plane resulting from the interference between two light waves can be written as a short-term average $I = \langle \{E_1(t) + E_2(t)\}^2 \rangle$, where $E_1(t)$ and $E_2(t)$ are the instantaneous electric fields generated by the waves from the two interfering light sources, and the average is taken over a time that is large compared with the period of a light wave, but small compared with the time-scale of the signals of interest.

The light at the detector in our system is the sum of the light propagating along the reference arm and the light propagating along the signal arm of the interferometer as presented in Fig. 2. Ignoring the phase change due to the propagation of the light along its path, the light from the reference arm can simply be expressed as.

$$E_{ref}(t) = A\cos(\omega t) \tag{1}$$

whereas the light for the signal arm is given by.

$$E_{sig}(t) = B(t)\cos(\omega t + kt + \Delta + \varphi(t)) \tag{2}$$

where E_{ref} and E_{sig} represents the electric field component of the reference and signal arm light, respectively, t is time, A and $B(t)$ are the amplitudes of the reference and signal light beam, respectively (where the signal is shown as time dependent because the modulator may introduce amplitude/intensity modulation as well as phase modulation), ω is the angular frequency of the light, kt is the term for the continuous phase change resulting from the piezoelectric scan mirror, Δ is the system optical path difference which results from the system construction process, and $\varphi(t)$ is the time dependent phase modulation induced by the LC device.

Assuming that the photodiode is not responsive to the frequency of the light, but has a sufficient bandwidth to respond to the modulating signals, then based on Eq. (1) and Eq. (2), the light intensity can be determined by calculating the average of the square of the sum of these two equations, which leads to the following:

$$I = \frac{A^2}{2} + \frac{B(t)^2}{2} + A{\cdot}B(t)\cos(kt + \Delta + \varphi(t)) \tag{3}$$

where the average is taken over a period that is much shorter than that of the modulating signals.

First of all, let us consider the case when there is no modulation. In this case, the signal will simply be an offset sine wave, as can be seen in Fig. 3 (a). Here we choose four specific points where the phase term, $kt + \Delta$, is equal to $n\pi$ and $\frac{\pi}{2} + n\pi$, labelled as I_x, I_y, I_z, and I_k in Fig. 3 (a).

At the corresponding four specific points labelled in Fig. 3(a), the intensity becomes:

$$I_x(t) = \frac{A^2}{2} + \frac{B(t)^2}{2} + A{\cdot}B(t)\cos(\varphi(t)) \tag{4}$$

$$I_y(t) = \frac{A^2}{2} + \frac{B(t)^2}{2} - A{\cdot}B(t)\sin(\varphi(t)) \tag{5}$$

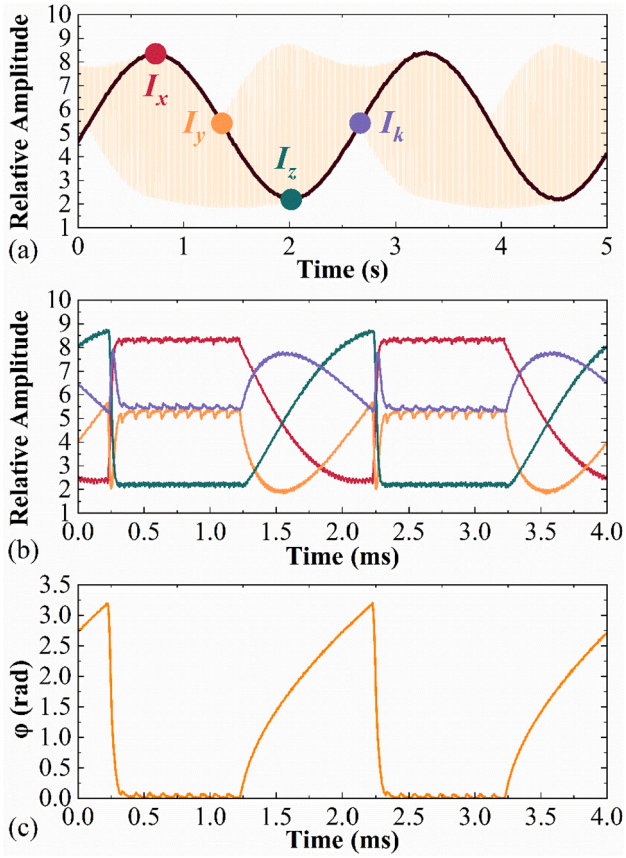

Fig. 3. (a) Example waveforms of the interference signal and the specific points of interest. The black solid line depicts the sine wave obtained when an LC phase modulator is placed in the signal arm but not modulated by an external electric field and the light yellow is an example envelope of the signal modulated by the LC device. (b) The realigned extracted signals from around the four specific points highlighted in (a). The dark red solid line is the waveform around I_x; the orange solid line represents the waveform around I_y; the dark green solid line is the waveform around I_z; and the purple line is the waveform around I_k. (c) An example of the time-resolved modulation of the optical phase of a 5 μm E7 nematic pi-cell when subjected to an applied voltage of $V = 10$ V at room temperature. The device was driven with a 5 kHz square wave, which is itself amplitude modulated with a second lower frequency wave that results in 1 ms duration bursts of the 5 kHz signal, followed by 1 ms spacings whereby $V = 0$ V. This data has been extracted according to Eq. (8). (The sample rate used for the data presented here is 200,000 per second.).

$$I_z(t) = \frac{A^2}{2} + \frac{B(t)^2}{2} - A \cdot B(t)\cos(\varphi(t)) \tag{6}$$

$$I_k(t) = \frac{A^2}{2} + \frac{B(t)^2}{2} + A \cdot B(t)\sin(\varphi(t)) \tag{7}$$

Subtracting (5) from (7) and (6) from (4) separately, and then dividing, we can obtain the value of the phase modulation from:

$$\varphi(t) = \arctan\left[\frac{I_k(t) - I_y(t)}{I_x(t) - I_z(t)}\right] \tag{8}$$

It should also be noted that.

$$A^2 + B(t)^2 = I_x(t) + I_z(t) \tag{9}$$

In practice, it is necessary to identify and select the data around the points labelled in Fig. 3(a) when a modulating signal is applied to the device. In order to do this, well defined reference points are added to the modulating signal. In post-processing, these can then be identified, and the signals can then be extracted from the points labelled and can then be "processed" using Eq. (8). The extracted and realigned data subsets from around the points I_x, I_y, I_z, and I_k are shown in Fig. 3(b). The resulting extracted optical phase as a function of time is then of the form shown in Fig. 3(c), the details relating to its shape and values will be analysed and discussed in the following sections. The raw data was collected by an A/D converter with a 200000-point-per-sec sample rate, allowing sufficient resolution to study the LC phase modulation.

2.2.2. Modelling of the LC director

The number of LC molecules is enormous even in a device of a few microns thickness, therefore simulation at an atomistic or molecular level is not appropriate in this case. Thus, a macroscopic continuum method based on Ericksen-Leslie-Parodi's [34–36] theory has been used for the simulations of the phase modulation. The LC director is thus treated as continuous which allows gradients to be specified. In many simulations that are undertaken for interpreting the switching behavior of nematic LC devices, the influence of backflow is not commonly discussed in detail. Some literature have discussed how backflow can influence the dynamics in nematic LC disclinations [37] and twist cell configurations [38]. However, for a rigorous understanding of the modulation, the backflow cannot be ignored, and the flow gradients have a significant impact on the dynamic behavior of the system. Generally, backflow has a negative impact on the switching times in a Fréedericksz device due to the flow-reorientation coupling but can have a more positive impact on the performance of a pi-cell. In their work, Walton and Towler make direct comparison between pi-cell switching times with and without the inclusion of flow-reorientation coupling in simulations [27] where it is shown that when the backflow is not included a slower switching response is observed in the pi-cell. This work therefore emphasises the importance and positive benefit of backflow effects in pi-cell switching. Taking these findings into consideration, the modelling in this work simulates the Frank elastic energy density function(s), as well as the effects of dielectric coupling and backflow. A numerical approach is then employed to determine the phase modulation behavior.

The director profile of a volume of LC material is defined in this work based on the coordinate system illustrated in Fig. 4. Here the structures under consideration are untwisted, and $\phi = 0$ and the director remains in the x-z plane. The HAN cell is intrinsically untwisted due to the homeotropic anchoring at one surface. Therefore, in such a device, when using an achiral nematic LC, the director is confined to a single switching plane. The Fréedericksz device has a small surface tilt angle of 4°, but is untwisted, although in practical devices small errors in device assembly can lead to small twists within the device. In this work devices are carefully chosen that show very little residual twist. Additionally, relatively high amplitude electric fields are applied in this work, ensuring that the director is perpendicular to the substrates in the centre of the cell, hence effectively decoupling the top and bottom halves of the cell – hence the assumption that the director remains in the x-z plane is reasonable. The pi-cells studied in this paper also have small surface tilt angles of 4°, and in these devices twisted states can occur when the

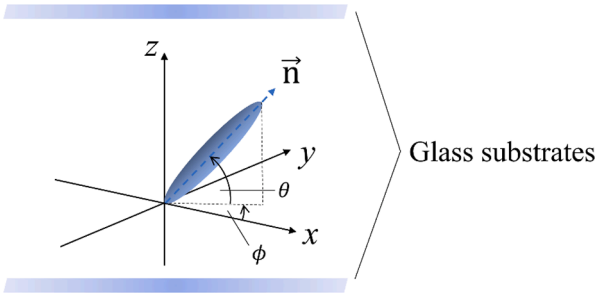

Fig. 4. The geometry of the LC director in a glass cell. The two substrate surfaces are in the x-y plane and are perpendicular to the z-axis.

electric field is removed. However, such states take time to form, and do not occur on the timescales of the modulation investigated here. Again, the top and bottom halves of the device are effectively decoupled by applying relative high amplitude electric fields, and the assumption that the director remains in the *x*-*z* plane is reasonable. The general Frank elastic energy density equation is then given by [39].

$$f_{elastic} = \frac{1}{2}K_{11}[\vec{\nabla}\cdot\vec{n}]^2 + \frac{1}{2}K_{22}[\vec{n}\cdot(\vec{\nabla}\times\vec{n}) - q]^2 + \frac{1}{2}K_{33}[\vec{n}\times(\vec{\nabla}\times\vec{n})]^2 \tag{10}$$

where K_{11}, K_{22}, K_{33} represent the splay, twist and bend elastic constants, respectively, and q is the natural twist of the material which is nonzero only in the chiral nematic phase and is equal to $\frac{2\pi}{p}$, where p is the pitch of a chiral nematic LC. The materials used in this study are not chiral, so $q = 0$. The electric field is applied across the cell, parallel to the *z*-axis in Fig. 4, and perpendicular to the substrates. The size of the active electrodes of the cells in the *x*-*y* plane was around 2.5 cm^2 whereas the cell gaps were under 10 μm. Therefore, because of the large aspect ratio between the length scale in the *z*-direction and the length scales in the *x*-*y* plane, the electric field $\vec{E}$ can be considered as consisting of only the component E_z, while $E_x = E_y = 0$. The electrostatic energy density of the device then takes the form.

$$f_{electro} = -\frac{1}{2}\vec{D}\bullet\vec{E} = -\frac{1}{2}D_zE_z = -\frac{1}{2}\varepsilon_0\varepsilon_{zz}{E_z}^2 \tag{11}$$

where ε_0 and ε_{zz} represent the free space permittivity and the *z*-component of the relative dielectric permittivity tensor, respectively, $\vec{D}$ is the electric field displacement vector and $\vec{E}$ is the electric field vector. In our system this becomes.

$$f_{electro} = -\frac{1}{2}{E_z}^2\varepsilon_0(\Delta\varepsilon\sin\theta^2 + \varepsilon_\perp) \tag{12}$$

With the large pixel assumption $\frac{\partial D_x}{\partial z} = \frac{\partial E_x}{\partial z} = \frac{\partial E_y}{\partial z} = 0$. The objective of the simulation is to determine how the LC alignment behavior changes over time, so using a computational method to solve the rate of the change of the free energy of the system is essential. The approach is to describe the rate of the energy dissipation as.

$$\frac{\partial}{\partial z}\left(\frac{\partial L}{\partial \dot{\theta}}\right) - \frac{\partial L}{\partial \theta} = \frac{\partial \mathscr{D}}{\partial \dot{\theta}} \tag{13}$$

where L is the free energy density, and $\mathscr{D}$ is the dissipation function.

Using the standard Einstein summation convention, the general form of the dissipation function, can be written as [40].

$$\begin{aligned}\mathscr{D} = &\left(\frac{\alpha_4}{4}\right)\left(v_{j,i}v_{j,i} + v_{j,i}v_{i,j}\right) + \left(\frac{\alpha_5-\alpha_2}{4}\right)\left(n_in_jv_{k,i}v_{k,j} - 2\dot{n}_kn_iv_{k,i}\right)\\ &+\left(\frac{\alpha_2+2\alpha_3+\alpha_5}{4}\right)\left(n_in_jv_{i,k}v_{j,k} - 2\dot{n}_kn_iv_{i,k}\right)\\ &+\left(\frac{\alpha_2+\alpha_5}{2}\right)\left(n_in_jv_{k,i}v_{j,k} + \dot{n}_kn_iv_{k,i} - \dot{n}_kn_jv_{j,k}\right) + \left(\frac{\alpha_1}{2}\right)n_in_jn_kn_pv_{j,i}v_{p,k}\\ &+\left(\frac{\alpha_3-\alpha_2}{2}\right){\dot{n}_k}^2\end{aligned}$$

where the $\alpha_1 \sim \alpha_5$ coefficients are the Leslie viscosities [35]. Assuming in a real device the LC flow is incompressible, then the only non-zero flow terms are the velocity of the fluid, $v_{x,z} = v_x'$. Substituting for the nematic LC configurations introduced here we then have.

$$\frac{\partial \mathscr{D}}{\partial \dot{\theta}} = (\alpha_3 - \alpha_2)\dot{\theta} + v_x'(\alpha_3\cos^2\theta - \alpha_2\sin^2\theta) \tag{14}$$

For the right-hand side of Eq. (14) there are two unknowns ($\dot{\theta}$, v_x'). Therefore, it is necessary to introduce the Navier-Stokes equation.

$$\rho\dot{v}_i = F_i + \sigma_{ji,j} \tag{15}$$

where ρ is the density of the fluid, $\dot{v}_i = \frac{\partial v_i}{\partial t}$, F_i is the external body force, and σ_{ji} is the stress tensor. It is assumed that in our system the external body force can be neglected, as a result, $F_i = 0$. Additionally, for the left-hand side of Eq. (15), it is assumed that inertial terms only act over a timescale significantly shorter than the relaxation time of the LC director. Thus, Eq. (15) is further reduced to $\sigma_{ji,j} = 0$. In this study, the only non-zero dynamic portion of the stress tensor in an untwisted nematic system is $\widetilde{\sigma}_{zx}$, which is given as.

$$\begin{aligned}\widetilde{\sigma}_{zx} = \frac{\partial \mathscr{D}}{\partial v'_x} = \frac{v'_x}{2}\Big[2\alpha_1\sin^2\theta\cos^2\theta + \alpha_2(\cos^2\theta - \sin^2\theta)\Big)\\ + 2\alpha_3\cos^2\theta + \alpha_4 + \alpha_5] + \dot{\theta}(\alpha_3\cos^2\theta - \alpha_2\sin^2\theta)\end{aligned} \tag{16}$$

Eq. (16) can now be combined with Eq. (14) to obtain a pair of equations for $\dot{\theta}$ and v'_x [41] – this system can then be solved numerically to determine the behavior of the LC director. Furthermore, based on the time dependence of the director profile, the intensity modulation can also be modelled along with the phase modulation using a Jones matrix approach to represent the light propagation through the nematic LC layer. The elastic, dielectric and refractive index coefficients used for the model here were $K_{11} = 11.1$ pN, $K_{33} = 17.1$ pN, $\varepsilon_\perp = 5.4$, $\varepsilon\| = 17.4$, $n_o = 1.5$, $n_e = 1.72$ and the wavelength was set to $\lambda = 632.8$ nm [42].

3. Results and discussion

The devices investigated here are three different, but well-known, configurations of nematic LC devices: a Fréedericksz cell [24], a pi-cell [24], and a HAN cell. In each case, the LC modulators are placed in the signal arm of the Michelson interferometer arrangement illustrated in Fig. 2. Each device is typically driven with a 5 kHz square wave, which is itself amplitude modulated with a second lower frequency wave. In the data presented in the following, this configuration is used in order to provide 1 ms duration bursts of the 5 kHz signal, followed by 1 ms "gaps" at 0 V. An example of the driving signal is shown in Fig. 5(a). The voltage amplitude used in this case is $V = 25$ V.

Alongside the driving waveform, Fig. 5 also shows a set of data that demonstrates the time-resolved phase modulation behavior of a 5 μm nematic pi-cell at room temperature. The phase modulation response shown in Fig. 5(b) is a result of the on–off external electric field which is shown in Fig. 5(a). It can be seen in Fig. 5(b) that a phase depth of around 3.7 rad is achieved over a timescale of 1 ms. Following the switch on state is a 1 ms period when the LC device is switched off (this is represented by the black line parts in Fig. 5(b)) where the LC device modulates the phase of the incident light from 0 to 3.7 rads in 1 ms (see, for example, the response over the time period from 1.5 ms to 2.5 ms in Fig. 5(b)), before rapidly dropping back to 0 rad when the electric field is re-applied. This behavior would easily lead to a phase modulation that was greater than 2π with a sub-millisecond timescale using the four-pass configuration that was presented in a previous paper [22].

Because the nematic pi-cell behaves as a capacitor, which is driven through the resistance of the indium tin oxide (ITO) electrodes, when the electric field reverses at 5 kHz between 25 V and −25 V, the capacitor charging time leads to a ripple in the signal which is the red line in Fig. 5(b). It is more noticeable in Fig. 5(c) when the voltage driving conditions were set to a square wave of $V = 25$ V, $f = 5$ kHz, but without the 500 Hz amplitude modulation. Fig. 5(d) shows the residual intensity modulation. The data shown in Fig. 5(d) was extracted using Eq. (9).

To investigate the behavior of the three different nematic LC devices, a series of experimental tests were carried out and the measurements were then compared with the results from simulations. In the simulations, the surface anchoring conditions are "strong", with a no-slip condition in the flow at the surfaces and infinity strength surface tilt anchoring with a small surface pretilt angle of 4°. The Leslie coefficients used in the model were $\alpha_1 = -21$ mPa·s, $\alpha_2 = -282$ mPa·s, $\alpha_3 = -1$

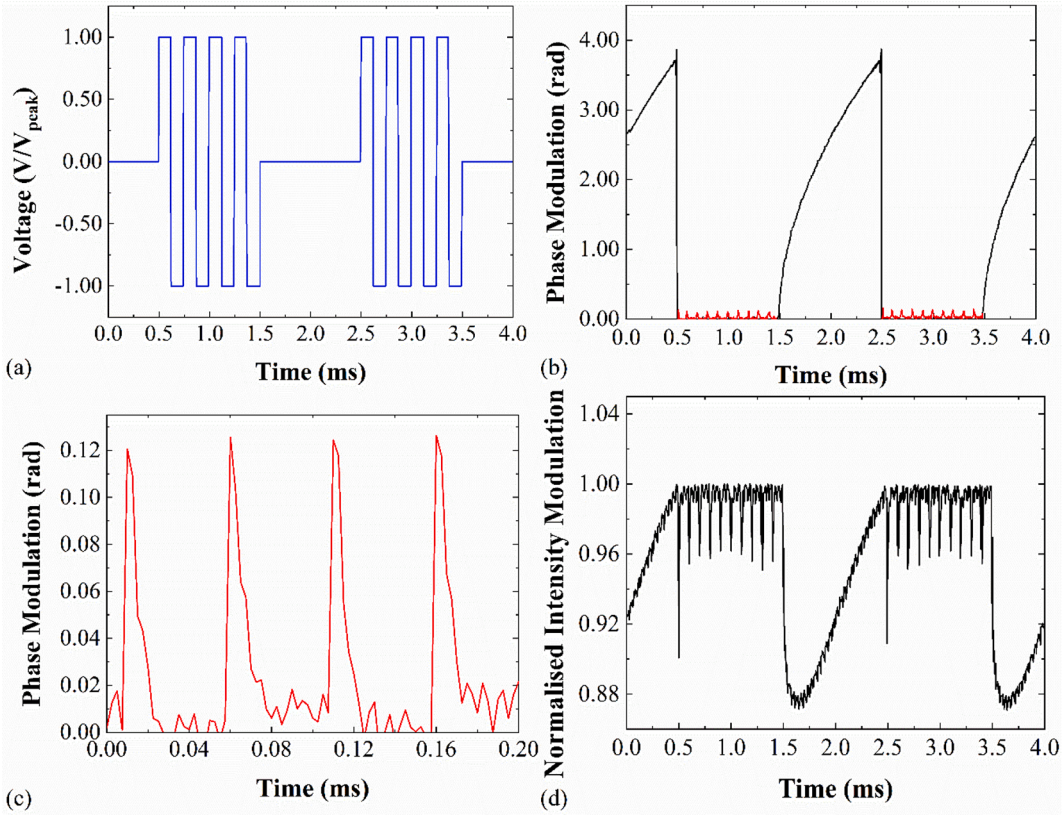

Fig. 5. An example of the experimental data for the time dependence of the phase modulation for a nematic LC pi-cell with a thickness of 5 μm. (a) An example of the modulated square wave, the square wave frequency is 5 kHz and the amplitude modulated (AM) frequency is 500 Hz. Note that the voltage amplitude is varied depending on the experiment and the value is specified in each case. (b) The extracted phase modulation using Eq. (8) as a function of time for the electric field conditions: $V = 25$ V and f = 5 kHz, AM frequency 500 Hz and (c) $V = 25$ V, f = 5 kHz without the application of the AM square wave. (d) corresponding intensity modulation as a function of time for a modulated square wave, $V = 25$ V, AM frequency 500 Hz. The value of the intensity has been normalized to the maximum intensity value.

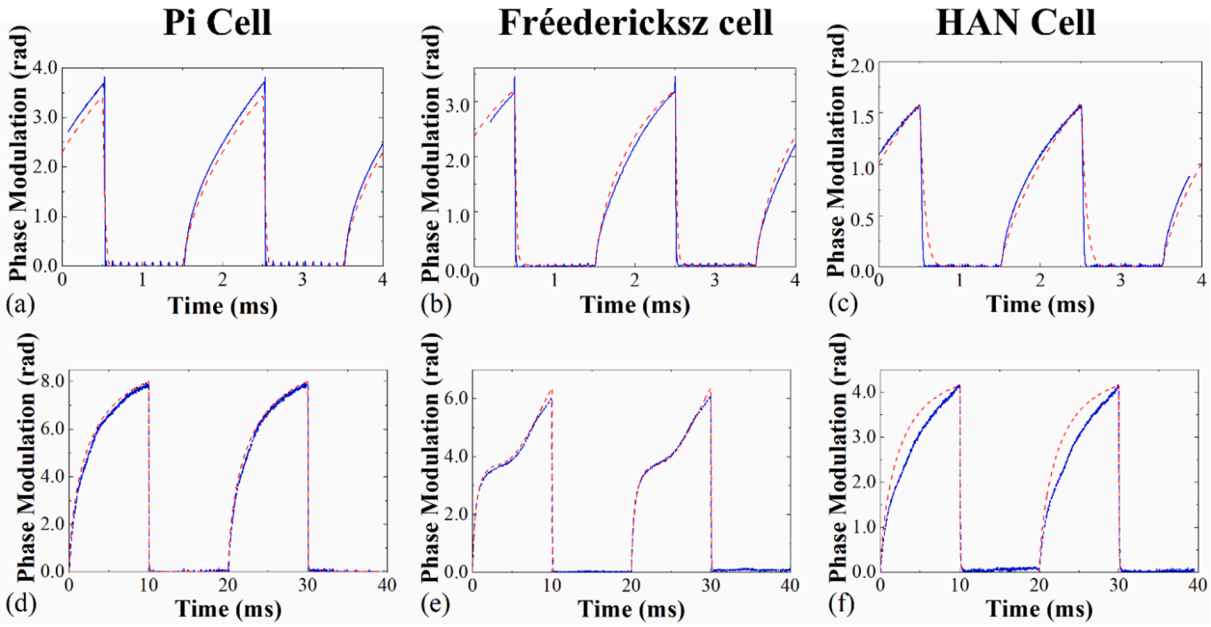

Fig. 6. Experimental measurements (blue solid lines) and simulations (red dashed lines) of the phase modulation as a function of time for the three different nematic LC configurations considered in this study: nematic pi cell (parallel rubbed alignment layers), Fréedericksz device (anti-parallel rubbed alignment layers), and a hybrid aligned nematic (HAN). The cell gap used in the simulation for the pi and Fréedericksz cells were 5.78 μm and 5.12 μm, respectively, whereas for the HAN cell, the thickness was 7.44 μm. Each cell was filled with the nematic LC, E7. The time when the modulating signal is applied and when the voltage is zero in (a), (b) & (c) were 1 ms, but were 10 ms in (d), (e) & (f). The amplitude of the applied voltage in all cases was $V = 25$ V. Measurements were carried out at room temperature.

mPa·s, $\alpha_4 = 225$ mPa·s and $\alpha_5 = 92$ mPa·s, taken from Ref. [43]. Fig. 6 shows direct comparisons between the experimentally determined phase modulation and the phase modulation predicted from simulations. Two sets of results are shown, one with an AM modulating frequency of 500 Hz (i.e., with the 5 kHz signal on for 1 ms, and off for 1 ms) (Fig. 6(a) – (c)), and one with an AM frequency of 50 Hz (i.e., with the 5 kHz signal on for 10 ms, and off for 10 ms) (Fig. 6(d) – (f)). The behavior for 1 ms bursts illustrates the available phase modulation over a target time scale of 1 ms, whereas the response for the 10 ms bursts serves to illustrate the impact of backflow on the resulting device behavior.

The results from simulations are found to be in good agreement with the experimental results for the different switching conditions. It can be seen that the shapes of the phase modulation response are very similar for all three devices when driven with 1 ms bursts. Furthermore, the nematic pi-cell (parallel rubbed) and the Fréedericksz device (anti-parallel rubbed) show similar phase modulation over a timescale of 1 ms (Fig. 6(a) and 6(b)), with the Fréedericksz device being just slightly less responsive. In contrast, the HAN device shows somewhat less phase modulation (Fig. 6(c)), and is thus less promising for commercial phase modulation technology.

The behavior observed can be understood in terms of the high voltage response of nematic LC devices. When high voltages are applied, the LC director in the bulk of the device is switched to a near homeotropic alignment. When the voltage is removed, however, the device returns towards the corresponding pi, planar or HAN states, depending upon the original configuration of the nematic LC. Initially, this relaxation occurs as boundary layer regions growing from planar-aligned surfaces [22]. In the nematic pi-cell and the Fréedericksz device these boundary layers grow from both surfaces, but in the HAN device, this only occurs at one surface, the corollary of which is that the level of phase modulation obtained is lower (compare Fig. 6(c) with Fig. 6(a) and 6(b)). This behavior is largely independent of the device thickness.

At longer time scales, however, the backflow becomes important, as is evident in the response of the devices when driven with 10 ms bursts (Fig. 6(d) – (f)). In these cases, we see substantially different responses between the pi-cell (Fig. 6(d)) and the Fréedericksz (Fig. 6(e)) devices. For the Fréedericksz device, it can be seen that the phase modulation increases rapidly when the field is removed before increasing at a slower rate up until approximately 5 ms when the phase modulation increases at a greater rate. This behavior is also reproduced in the simulations and is an effect that is caused by backflow, which tends to hinder the switch-off response in Fréedericksz devices. This behavior is not apparent in the pi-cells because in these devices the backflow tends to work with the switch-off response (i.e., with the reorientation of the director) rather than against it. As noted above, this concept has been demonstrated previously in the work of Walton and Towler where direct comparison was made between the flow influenced pi-cell director relaxation and the behavior observed when ignoring flow [27].

It is clear that the limiting effect in terms of the available phase modulation depth is the phase change that occurs during the switch-off period after the device has been driven on. Therefore, we further investigated the available phase modulation depth of the devices under different applied voltages. Five experimental points were chosen, with the driving voltages varying from $V = 5$ V to $V = 25$ V in increments of 5 V. The magnitude of the deviation between the theory and the measurement was 0.14 rads for the HAN cell and 0.09 rads for pi and Fréedericksz cells.

Fig. 7 presents both experimental and modelling results of the achievable phase modulation depth as a function of the applied voltage amplitude. The waveform that was applied was the same shape as that illustrated in Fig. 5(a) and here the black squares represent the results from simulations while the red dots represent the experimental results at the five different voltages. The results also show that for the same applied voltage amplitude, the nematic pi cell performs best in terms of the available phase modulation compared with both the Fréedericksz cell and the HAN cell. Similarly, and as shown here, the pi-cell can achieve more than a π ($\phi = 3.14$ rads) phase modulation (or 2π phase modulation if the device is implemented in a four-pass configuration of the type discussed in Ref. [22]) at a lower voltage amplitude ($V = 6.9$ V) and can achieve the largest phase modulation of all three devices ($\phi = 3.7$ rads). For the nematic pi-cell and the Fréedericksz device, the dashed

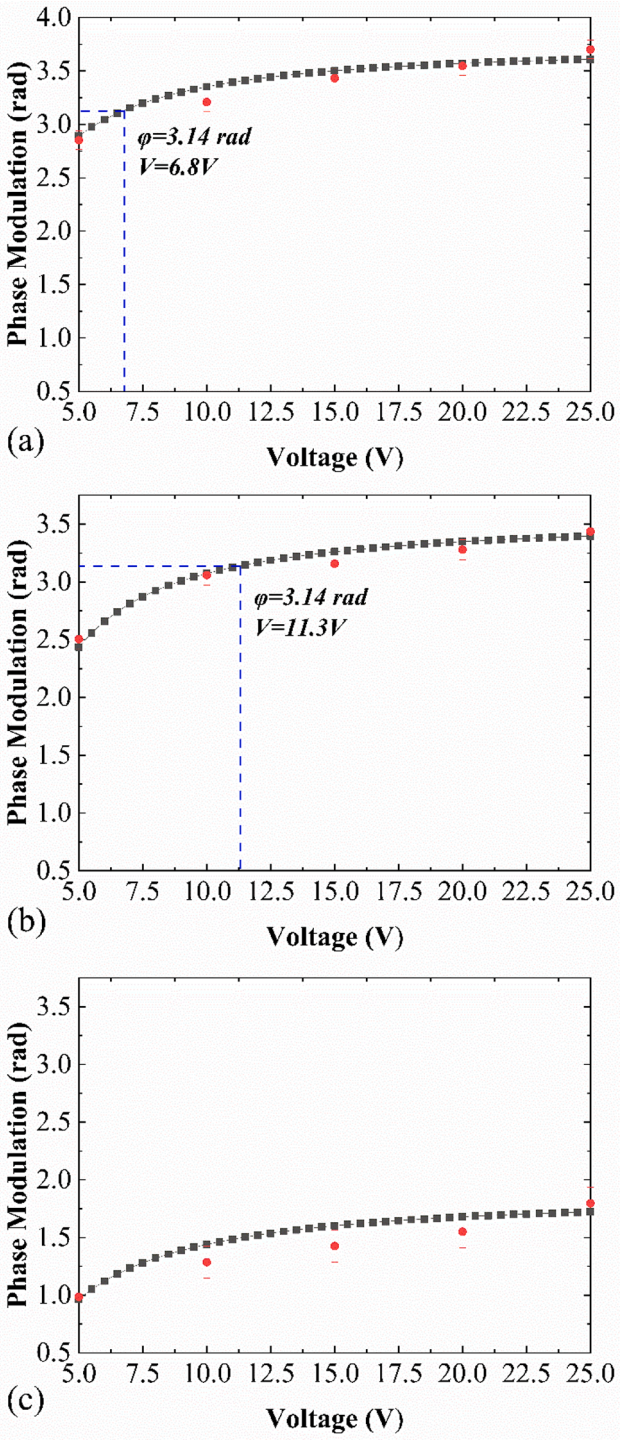

Fig. 7. The available phase modulation as a function of voltage when driven with voltage waveforms of the same shape as that shown in Fig. 5(a). The black squares represent the simulation results and the red dots represent the experimental results recorded at five different voltage amplitudes for the switching on state. (a) a nematic pi cell, (b) a Fréedericksz cell, and (c) a HAN cell. The experimental results were obtained at room temperature.

blue lines in the plot indicate the voltage that corresponds to a π phase modulation. It can also be seen that the HAN cell used here cannot reach a full π phase modulation in a timescale of 1 ms, even though the cell thickness is more than that of the pi-cell and Fréedericksz cell. For each configuration, as the drive voltage is increased, the phase modulation increases, but above a certain level the increase is only very small. This is because once the applied voltage reaches a level such that the boundary layer between the bulk homeotropic state and the planar surface state is substantially less than the wavelength of light, a further voltage increase does not substantially increase the change in the phase.

Finally, we illustrate experimental measurements of the time-dependent behavior of the phase modulation when switching between arbitrary phase modulation depths for the nematic LC pi-cell. In this case, the applied 5 kHz square wave is modulated by a pseudo-random pattern, and the resulting time-dependent phase was extracted. This is shown in Fig. 8. The electric field was set such that the waveform was the same form as that shown in Fig. 5(a), and the amplitude of the applied voltage was varied every 1 ms, which can be seen in the yellow plane in Fig. 8. A voltage sequence was then applied as follows: the voltage is switched on (the dark red areas), a lower voltage that behaves as a switch off voltage (the lightest red areas) and then a hold voltage (the red color bar in between). The director will remain at a certain orientation that results in a specific, steady phase modulation for 1 ms when subjected to the voltage sequence. By adjusting the relative value of voltage amplitude during the three periods, the phase modulation can be varied on demand. Fig. 8 clearly shows that for a practical phase modulation application scenario, the phase can still be modulated by up to 3.7 rads within a sub-millisecond timescale. Therefore, it is seen that the available pseudo-random phase modulation is consistent with the range observed above.

4. Conclusion

In this paper, we have presented a method to experimentally measure the time-dependent phase modulation of liquid crystal (LC) devices. This method was then used to study and characterise the response of three different nematic LC devices: pi-cell (parallel-rubbed alignment layers), Fréedericksz cell (anti-parallel rubbed alignment layers), and a hybrid aligned nematic (HAN) LC. The results presented have shown that both the intensity and phase properties can be determined by simply recording and analysing the signal captured by the photodiode in a Michelson interferometer when the reference arm is modified to provide a phase ramp. In order to understand fully how the alignment configuration and the initial director orientation of the LC can affect the phase modulation behavior, simulations were conducted based upon the Frank elastic energy density, effects of dielectric coupling, and importantly, the impact of backflow.

In this study, a range of device driving voltages have been explored, with driving voltages up to 25 V. For the nematic LC E7 in each of the three different configurations, the "useful" range of driving voltages was determined, defined here as when a π phase modulation is achieved in the test arrangement discussed above. A π phase modulation was achieved at a driving voltage of 6.8 V for the nematic pi-cell, compared with 11.3 V for the Fréedericksz device. However, a π phase modulation was not achieved in the HAN cell. These results would lead to full 2π phase modulation in a four-pass configuration [22] for the pi and Fréedericksz devices at reasonable driving voltages (less than 10 V in the case of the pi-cell). In contrast, the HAN cell did not reach a π phase modulation despite the LC layer being somewhat thicker. It was also shown that when backflow was prevalent there was a negative impact on the dynamic phase response of the Fréedericksz device but not the pi-cell. The experimental results and simulations both suggest that the pi-cell is potentially better suited for phase modulation when fast switching speeds and a wide phase change are required.

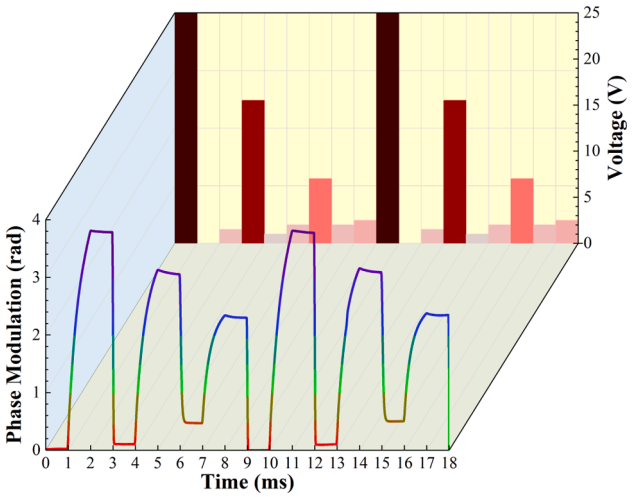

Fig. 8. The phase modulation as a function of time for the nematic pi-cell in an arbitrary phase-modulation sequence. The plot on the yellow panel represents the rms voltage applied to the cell and the applied waveform is a 5 kHz square wave but in this case, the amplitude changes every 1 ms according to the plot on the yellow panel. The darker red bars indicate a higher voltage amplitude. Each red bar is 1 ms in duration and the corresponding relative phase shift is shown in the front panel, where the color of the line reflects the depth of the modulated phase. The purple parts indicate that the modulation is greater than π. The phase modulation changes along with the 'switch on– switch off- hold' electric field sequence so that the phase depth is lowest (red parts) at first and then increases to a high value (the gradient changes color from red to green to purple or blue) and then remains held at that level for another 1 ms without any significant change (the purple or blue parts). Hence, by controlling the amplitude modulation of the applied waveform, different levels of phase modulation can be achieved.

CRediT authorship contribution statement

Yihan Jin: Conceptualization, Validation, Investigation, Visualization, Writing – original draft. **Steve J. Elston:** Conceptualization, Methodology, Data curation, Supervision, Writing – review & editing. **Julian A.J. Fells:** Methodology, Conceptualization, Writing – review & editing. **Bohan Chen:** Resources. **Mengmeng Li:** Resources. **Waqas Kamal:** Resources. **Zimo Zhao:** Resources. **Stephen M. Morris:** Supervision, Conceptualization, Project administration, Writing – review & editing, Funding acquisition.

Declaration of Competing Interest

The authors declare that they have no known competing financial interests or personal relationships that could have appeared to influence the work reported in this paper.

Data availability

Data will be made available on request.

Acknowledgement

This research was supported by the Engineering and Physical Sciences Research Council (UK) (grant number EP/M017923/1). W. K. gratefully acknowledges the Punjab Education Endowment Fund for a graduate scholarship.

References

[1] R.J. Beck, J.P. Parry, W.N. Macpherson, A. Waddie, N.J. Weston, J.D. Shephard, D. P. Hand, R.R. Beck, J. Carrington, W. Parry, A. Macpherson, D.T. Waddie, N. Reid, J. Weston, D.P. Shephard, Application of cooled spatial light modulator for high

power nanosecond laser micromachining, Opt. Express 18 (2010) 17059–17065, https://doi.org/10.1364/OE.18.017059.
[2] S. Ahderom, M. Raisi, K. Lo, K.E. Alameh, R. Mavaddat, Applications of liquid crystal spatial light modulators in optical communications, in: In: 5th IEEE International Conference on High Speed Networks and Multimedia Communication, 2002, pp. 239–242, https://doi.org/10.1109/HSNMC.2002.1032583.
[3] J. Kubby, S. Gigan, M. Cui (Eds.), Wavefront Shaping for Biomedical Imaging, Cambridge University Press, 2019.
[4] N. Matsuda, A. Fix, D. Lanman, Focal surface displays, ACM Trans. Graph. 36 (4) (2017) 1–14.
[5] A. Maimone, A. Georgiou, J.S. Kollin, Holographic near-eye displays for virtual and augmented reality, ACM Trans. Graph. 36 (4) (2017) 1–16.
[6] Y.-W. Li, C.-W. Lin, K.-Y. Chen, K.-H. Fan-Chiang, H.-C. Kuo, H.-C. Tsai, 18.5L: Late-News Paper: Front-lit LCOS for Wearable Applications, SID Symposium Digest of Technical Papers. 45 (1) (2014) 234–236, https://doi.org/10.1002/j.2168-0159.2014.tb00064.x.
[7] Y. Huang, Z. He, S.-T. Wu, Fast-response liquid crystal phase modulators for augmented reality displays, Opt. Express 25 (26) (2017) 32757, https://doi.org/10.1364/OE.25.032757.
[8] H. Zhang, Z. Zhang, J. Lv, C. Peng, W. Hu, Fast beam steering enabled by a chip-scale optical phased array with 8 × 8 elements, Opt. Commun. 461 (2020) 125267, https://doi.org/10.1016/j.optcom.2020.125267.
[9] D.R. Gozzard, L.E. Roberts, J.T. Spollard, P.G. Sibley, D.A. Shaddock, Fast beam steering with an optical phased array, Opt. Lett. 45 (13) (2020) 3793, https://doi.org/10.1364/OL.393007.
[10] X. Gao, M. Zhao, M. Xie, M. Lei, X. Song, K.e. Bi, Z. Zheng, S. Huang, 2D optically controlled radio frequency orbital angular momentum beam steering system based on a dual-parallel Mach-Zehnder modulator, Opt. Lett. 44 (2) (2019) 255, https://doi.org/10.1364/OL.44.000255.
[11] S. Turtaev, I.T. Leite, K.J. Mitchell, M.J. Padgett, D.B. Phillips, T. Čižmár, Comparison of nematic liquid-crystal and DMD based spatial light modulation in complex photonics, Opt. Express 25 (24) (2017) 29874, https://doi.org/10.1364/OE.25.029874.
[12] T.J. Drabik, A.H. Titus, M.A. Handschy, D. Banas, S.D. Gaalema, D.J. Ward, 2D silicon/ferroelectric liquid crystal spatial light modulators, IEEE Micro 15 (1995) 67–76, https://doi.org/10.1109/40.400643.
[13] X. Wang, J.A.J. Fells, W.C. Yip, T. Ali, J. Lin, C. Welch, G.H. Mehl, M.J. Booth, T. D. Wilkinson, S.M. Morris, S.J. Elston, Fast and low loss flexoelectro-optic liquid crystal phase modulator with a chiral nematic reflector, Sci. Rep. 9 (2019) 7016, https://doi.org/10.1038/s41598-019-42831-5.
[14] T. Kurokawa, S. Fukushima, Spatial light modulators using ferroelectric liquid crystal, Optical and Quantum, Electronics. 24 (10) (1992) 1151–1163, https://doi.org/10.1007/BF00620311.
[15] C.J. Henderson, D.G. Leyva, T.D. Wilkinson, Free space adaptive optical interconnect at 1.25 Gb/s, with beam steering using a ferroelectric liquid-crystal SLM, J. Lightwave Technol. 24 (5) (2006) 1989–1997, https://doi.org/10.1109/JLT.2006.871015.
[16] M. Pivnenko, K. Li, D. Chu, Sub-millisecond switching of multi-level liquid crystal on silicon spatial light modulators for increased information bandwidth, Optics Express. 29 (2021) 24614. Doi: 10.1364/OE.429992.
[17] Z. Luo, F. Peng, H. Chen, M. Hu, J. Li, Z. An, S.-T. Wu, Fast-response liquid crystals for high image quality wearable displays, Opt. Mater. Express. 5 (3) (2015) 603, https://doi.org/10.1364/OME.5.000603.
[18] R.M. Hyman, A. Lorenz, S.M. Morris, T.D. Wilkinson, Polarization-independent phase modulation using a blue-phase liquid crystal over silicon device, Appl. Opt. 53 (29) (2014) 6925, https://doi.org/10.1364/AO.53.006925.
[19] Z. Zhang, G. Lu, F.T.S. Yu, Simple method for measuring phase modulation in liquid crystal televisions, Opt. Eng. 33 (1994) 3018, https://doi.org/10.1117/12.177518.
[20] H. Zhang, J. Zhang, L. Wu, Evaluation of phase-only liquid crystal spatial light modulator for phase modulation performance using a Twyman-Green interferometer, Meas. Sci. Technol. 18 (6) (2007) 1724–1728, https://doi.org/10.1088/0957-0233/18/6/S09.
[21] A.K. Gupta, N.K. Nishchal, Phase characterization of a liquid crystal spatial light modulator, in: In: 2018 3rd International Conference on Microwave and Photonics (ICMAP), 2018, pp. 1–2, https://doi.org/10.1109/ICMAP.2018.8354597.
[22] Y. Jin, S.J. Elston, J.A.J. Fells, M.J. Booth, C. Welch, G.H. Mehl, S.M. Morris, Millisecond optical phase modulation using multipass configurations with liquid-crystal devices, Phys. Rev. Appl 14 (2) (2020), https://doi.org/10.1103/PhysRevApplied.14.024007.
[23] J.A.J. Fells, P.S. Salter, C. Welch, Y. Jin, T.D. Wilkinson, M.J. Booth, G.H. Mehl, S. J. Elston, S.M. Morris, Dynamic phase measurement of fast liquid crystal phase modulators, Optics Express. 30 (2022) 24788. Doi: 10.1364/OE.460083.
[24] Z. Zhang, Z. You, D. Chu, Fundamentals of phase-only liquid crystal on silicon (LCOS) devices, Light Sci. Appl. 3 (10) (2014) e213.
[25] P.J. Bos, K.R. Koehler/beran, The pi-Cell: A Fast Liquid-Crystal Optical-Switching Device, Molecular Crystals and Liquid Crystals. 113 (1984) 329–339. Doi: 10.1080/00268948408071693.
[26] Y.i. Huang, P.J. Bos, K.H. Kim, J.K. Jang, H.S. Kim, Factors affecting the dynamics of a π-cell (Invited Paper), J Soc Inf Disp. 16 (9) (2008) 939, https://doi.org/10.1889/1.2976654.
[27] H.G. Walton, M.J. Towler, On the response speed of pi-cells, Liq. Cryst. 27 (10) (2000) 1329–1335, https://doi.org/10.1080/026782900423386.
[28] Y. Wang, X. Zhou, W. Ye, Z. Zhang, New surface order reconstruction induced by electric field application in a nanoconfined HAN cell with a topological defect, AIP Adv. 5 (10) (2015) 107127, https://doi.org/10.1063/1.4934672.
[29] A. Aizen, M. Ney, A. Safrani, I. Abdulhalim, A compact real-time high-speed high-resolution vibrometer, surface profiler and dynamic focus tracker using three wavelengths parallel phase-shift interferometry, Opt. Lasers Eng. 107 (2018) 304–314, https://doi.org/10.1016/J.OPTLASENG.2018.04.007.
[30] A. Nazarov, M. Ney, I. Abdulhalim, Compact and fast sub-nm scale displacement probe using a phase mask and parallel phase-shift interferometry, J. Phys. D Appl. Phys. 51 (33) (2018) 335102, https://doi.org/10.1088/1361-6463/aad265.
[31] A. Safrani, I. Abdulhalim, Real-time phase shift interference microscopy, Opt. Lett. 39 (17) (2014) 5220, https://doi.org/10.1364/OL.39.005220.
[32] W. Kamal, M. Li, J.-D. Lin, E. Parry, Y. Jin, S.J. Elston, A.A. Castrejón-Pita, S. M. Morris, Spatially Patterned Polymer Dispersed Liquid Crystals for Image-Integrated Smart Windows, Advanced, Opt. Mater. 10 (3) (2022) 2101748, https://doi.org/10.1002/adom.v10.310.1002/adom.202101748.
[33] J. Li, G. Baird, Y.-H. Lin, H. Ren, S.-T. Wu, Refractive-index matching between liquid crystals and photopolymers, J Soc Inf Disp. 13 (12) (2005) 1017, https://doi.org/10.1889/1.2150371.
[34] M.P. Allen, D. Frenkel, Calculation of liquid-crystal Frank constants by computer simulation, Phys. Rev. A 37 (5) (1988) 1813–1816, https://doi.org/10.1103/PhysRevA.37.1813.
[35] F.M. Leslie, Some constitutive equations for liquid crystals, Arch. Ration. Mech. Anal. 28 (4) (1968) 265–283, https://doi.org/10.1007/BF00251810.
[36] O. Parodi, Stress tensor for a nematic liquid crystal, J. Phys. 31 (7) (1970) 581–584, https://doi.org/10.1051/jphys:01970003107058100.
[37] C. Blanc, D. Svenšek, S. Žumer, M. Nobili, Dynamics of Nematic Liquid Crystal Disclinations: The Role of the Backflow, Phys. Rev. Lett. 95 (2005), 097802, https://doi.org/10.1103/PhysRevLett.95.097802.
[38] D.W. Berreman, Liquid-crystal twist cell dynamics with backflow, J. Appl. Phys. 46 (9) (1975) 3746–3751, https://doi.org/10.1063/1.322159.
[39] F.C. Frank, I. LIQUID CRYSTALS ON THE THEORY OF LIQUID CRYSTALS, Discussion of the Faraday Society. 25 (1958) 19–28. https://pubs.rsc.org/en/content/articlepdf/1958/df/df9582500019.
[40] G. Vertogen, W.H. de Jeu, Thermotropic Liquid Crystals, Fundamentals, Springer, Berlin Heidelberg, Berlin, Heidelberg (1988), https://doi.org/10.1007/978-3-642-83133-1.
[41] P. Brimicombe, E.P. Raynes, Fast-switching nematic liquid crystal devices, Thesis (D.Phil.), University of Oxford, 2006.
[42] C. Kischka, Flexoelectricity in nematic liquid crystals, Thesis(D.Phil.), University of Oxford, 2011.
[43] H. Wang, T.X. Wu, S. Gauza, J.R. Wu, S.-T. Wu, A method to estimate the Leslie coefficients of liquid crystals based on MBBA data, Liq. Cryst. 33 (1) (2006) 91–98, https://doi.org/10.1080/02678290500446111.